IPPI
Polyolefins Journal, Vol. 7, No. 1 (2020)
DOI: 10.22063/poj.2019.2568.1141

REVIEW PAPER

Simulation and modeling of macro and micro components produced by powder injection molding: A review

Rezvan Yavari[1], Hamid Khorsand[1*], Mehran Sardarian[2]

[1]Faculty of Materials Science and Engineering, K. N. Toosi University, Tehran, Iran
[2]Faculty of Materials and Metallurgical Engineering, Semnan University, Semnan, Iran

Received: 27 September 2019, Accepted: 24 November 2019

ABSTRACT

During the recent years powder processing technologies have gained much attention due to the less energy consumption and recyclable powders. Manufacturing of complicated parts by the conventional powder metallurgy (PM) method is hard due to the uniaxial pressure, which leads to the low design flexibility. In order to prevail these constraints, powder injection molding (PIM) process, which includes powder metallurgy and injection molding processes, is introduced. In powder injection molding, simulations are a very useful tool to predict each step of process and design the mold. By this way, design can already be optimized and mistakes are avoided. In this review a detailed study of simulation of different steps in the powder injection molding process of macro and micro components produced by this method is presented. Simulation investigations of mixing, injection, debinding, and sintering of various researchers are given. The computer simulation tools available for all steps of the PIM process are surveyed and results are presented. **Polyolefins J (2020) 7: 45-60**

Keywords: Powder injection molding, simulation, mixing, debinding, sintering, injection.

CONTENT

INTRODUCTION

Powder injection molding (PIM) is an affordable method for the manufacture of a wide range of macro and micro-scaled ceramic and metal parts and components. This process is a combination of polymer injection molding process and powder metallurgy technology in order to produce intricate metal and ceramic components. This process includes four main steps: mixing of powder and polymer, molding or injecting, remove

* Corresponding Author - E-mail: hkhorsand@kntu.ac.ir

of binder (debinding), and sintering [1-4]. Powders (usually <20 μm) and polymer binders are first mixed, then heated and injected in the molding machine, and when the binder freezes in the mold, the component is ejected. The binder supplies flowability to the feedstock [5]. Next, the binder should be removed by thermal debinding process or by solvent debinding process or combination of solvent and thermal debinding. The part obtained in this step is called brown part and should be sintered to near-full density. A vast range of materials, including metals, ceramics, and cemented carbides are studied to be manufactured by PIM. In powder injection molding, simulations are very beneficial tools to get information about the process before making the mold. Actually, simulation tools optimize the design and correct the possible defects in the part [6-8]. In PIM process material and process parameters should be optimized in order to manufacture defect-free parts. This is especially more critical for μPIM components. Actually, in μPIM process the prediction of behavior and optimization of process via computer simulation tools is more important. For example, micro-gear (a)[9], multi-slotted heat sink panel (b) [10] and miniature gas turbine stators (c)[11] are some powder injection molded parts which are shown in Figure 1. Table 1 shows some of high volume fabrication techniques. It is obvious that PIM process is a favorable method for the fabrication of intricate shapes with higher geometric precisions [12,13].

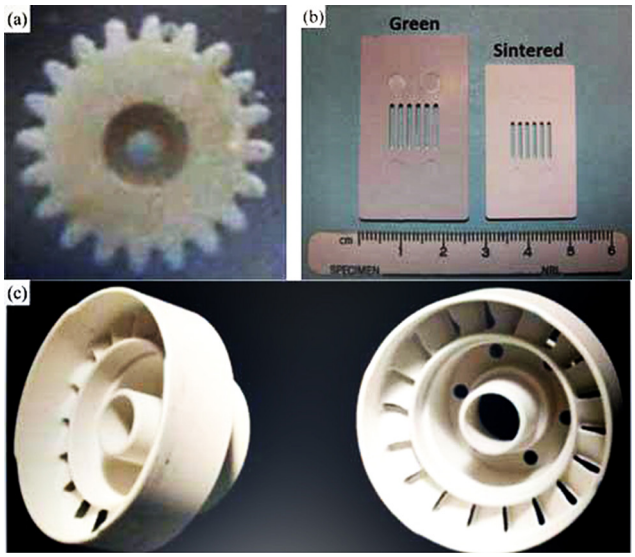

Figure 1. Some powder injection molded parts.

NECESSARY MATERIAL DATA FOR SIMULATION

Parameters such as density, thermal conductivity, and specific heat capacity are needed as the input data to perform PIM simulations. Furthermore, viscosity and specific volume should be measured in a range of shear rates and pressures, respectively [14].

Accurate and reliable simulation requires the properties of materials. Different stages such as filling, packing, and cooling are controlled by the flow of the feedstock.

Therefore, the following properties are required [15,16]:

- Viscosity
- Specific heat capacity
- Thermal conductivity
- No-flow temperature, glass transition, or melt temperature
- PVT data

No-flow temperature is one of the input parameters for simulation which is related to the rheological behavior of feedstock. According to this concept, the feedstock cannot flow under a certain temperature. Therefore, when this temperature is attained, the feedstock will flow during filling and packing [17].

Glass transition is another input parameter for simulation which can be determined through DCS (differential scanning calorimetry) test. Actually in the Cross-WLF model, discussed later, there is T^* parameter which is defined as the reference temperature and often the glass transition temperature of the polymer is applied for this parameter [18].

PVT is the abbreviation of the relation between

Table 1. Net-shape manufacturing processes for fabrication of engineering ceramics [8].

Parameters	PIM	Casting		Pressing	Machining
		Slip/tape	Robocasting		
High volume manufacturing	high	Low	High	Medium	Low
Density	95-100%	95-99%	95-99%	95-100%	100%
Geometric precision	High	Low	Medium	Low	Low
Shape intricacy	Yes	No	Yes	No	No
Wall thickness	10μm	>5mm	≥100μm	>2mm	>2mm
Ancillary machining	No	Yes	No	Yes	-

Table 2. Software summary from literature review [12].

Software	Solve	Type of analysis	Model
C-Mold	FEM	2D	Cross WLF
Moldflow	FEM	3D	Cross WLF, Second order
ProCAST	FEM	3D	Carreau Yasuda
Moldex	FVM	3D	Herschel Bulkley- Cross
Cadmould 3D-F	FEM	3D	Cross WLF, Carreau WLF
Sigmasoft	FEM	3D	Cross WLF- Herschel-Bulkley
PIM Solver	FEM/FDM	2.5D	Cross WLF

Pressure, Volume and Temperature. For the modeling of the evolution of density with pressure and temperature, the PVT data is needed. Since the compressibility factor of the feedstock during mold filling is lower than 10-9Pa, the fluid shows incompressible behavior. After the filling stage is completed, the assumption of incompressibility is not valid any more. PVT data is required because the pressure gradient at the packing stage is much higher. Dilatometer is used to obtain PVT data [19]. Some of the software tools used in the simulation PIM process are listed in Table 2 [19]. Some empirical models used for the estimation of physical, thermal and rheological properties of feedstocks are presented in Table 3 [14].

Xb and Xp are the mass fraction of binder and powder, respectivelly. ρc, ρb, and ρp are the density of feedstock, measured density of binder, density of powder, respectivelly. Cpc, Cpb and Cpp are the specific heat of feedstock, specific heat of binder system, and specific heat of powder, respectively. λ_c is the thermal conductivity of feedstock, $\lambda_{b\ exp}$ is the measured thermal of binder and λ_p is the thermal conductivity of filler.

Simulation of mixing

After the selection of desired materials (powder and binder), they should be mixed. To certify the manufacture of uniform products with favorable properties, homogeneity of the feedstock should be considered as the most important and critical parameter [16]. Kang et al. [15] used a particle tracking method and investigated mixing of powder injection molding feed-

Table 3. Some models for the estimation of feedstock properties [9].

Property	Empirical relations	#
Density	$\frac{1}{\rho_c}=\frac{X_b}{\rho_{b\,exp}}+\frac{X_p}{\rho_p}$	1
Volume fraction	$\phi_p=\frac{X_p\rho_P l}{X_P\rho_P+\mid X_b \mid \rho_{b\exp}}$	2
Specific heat	$C_{pc}=\left[C_{pb\,exp}X_b+C_{p_p}X_p\right]*\left[1+A*X_bX_p\right]$	3
Thermal conductivity	$1\text{-}\varnothing_p=\left(\frac{\lambda_p\lambda_c}{\lambda_p-\lambda_{b\,exp}}\right)\left(\frac{\lambda_b}{\lambda_c}\right)^{1/3}$	4
Viscosity	$\eta_c=\frac{\eta_0}{1+\left(\frac{\eta_0\gamma}{\tau^*}\right)^{1-n}}$	5
	$\eta_c=\frac{\eta_{b\,exp}}{[1-\frac{\varnothing_c}{\varnothing_{max}}]^2}$	
	$\eta_0=D_1\exp\left[-\frac{A_1\left(T-T^*\right)}{A_2+T-T^*}\right]$	

stock in a static mixer. They employed the capillary rheometry to measure the viscosity of feedstock then fitted data using the Cross-WLF model. The progress of mixing was qualitatively visualized in the down-channel direction via a particle tracking method and characterized using the information entropy. The typical geometry of the 6-element static mixer consisting of a circular pipe and the mixing elements twisted by 180o in alternating directions which is used in their simulations is illustrated in Figure 2. Figure 3 shows the progress in the first half period and with the blade rotating 180° in a counterclockwise direction. It can be seen that the mixing element (blade) has cut the two fluids horizontally and the split materials are deformed by the helical motion, which increases the number of striations at the end of the process. When the next half-period begins, the materials are cut vertically and the similar operations (stretching and stacking) are repeated. They used finite element method with the Cross-WLF (Williams-Landel-Ferry) model to solve the flow problem in their study. They assumed that homogeneous materials are used and the flow is only governed by viscous force and the inertia force is neglected.

As mentioned above, during the injection molding step the segregation of powder and binder in a homogeneous feedstock is minimum, and after the debinding and sintering an isotropic shrinkage will be obtained [20]. Jang et.al [20] evaluated the feedstock for powder injection molding and stated that the homogeneity of the feedstock can be investigated by a combination of: the ratio of feedstock weight loss during debinding, scanning electron microscopy (SEM) of the distribution of powder and binder, and pycnometric density of feedstock. They expressed that by increasing the shear rate, the inhomogeneity of feedstock increases.

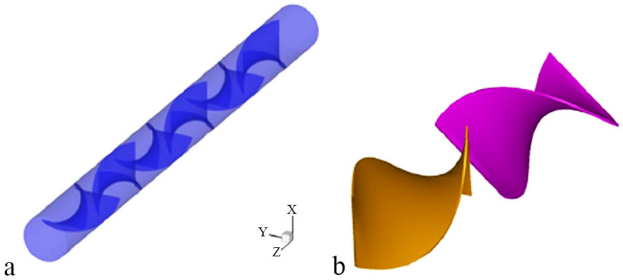

Figure 2. Simulation of mixing (a) hexa helical elements mixer, (b) LR-180 elements, mixing elements which are twisted 180o in intermittent directions [15].

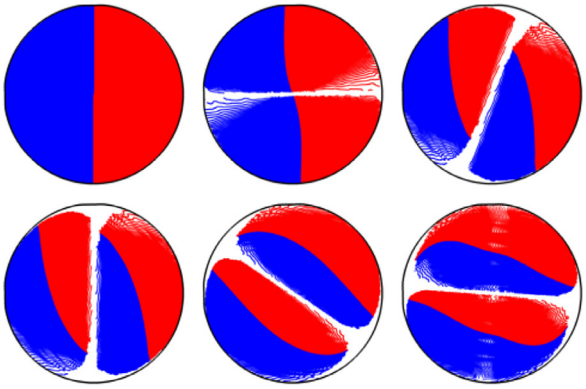

Figure 3. Working principle of the Kenics mixer. Colors show the mixing evolution, indicating fluid-particles mixtures for the first half period [15].

They used thermo gravimetric analysis (TGA) to determine the homogeneity and variations of feedstock weight. In another study, Askari et.al [21] investigated the rheological and thermal characterization of AISI 4605 low-alloy steel feedstock. They stated that proper solids loadings have an important effect on the homogeneity of feedstock, and separation of binder and powder. They used torque rheometer to measure the critical solids loading. For this purpose they added the powder to the binder system in a mixer and the mixing torque versus time was recorded at different solids loadings. They observed a linear increase in the mean torque value by increasing solids loading up to 58 Vol%. After that due to the friction of remaining powders in feedstock, the slop has changed (Figure 4).

In a similar research Abdoos et.al determined the proper solids loading of an aluminum feedstock. They defined CPVC (Critical Powder Volume Concentra-

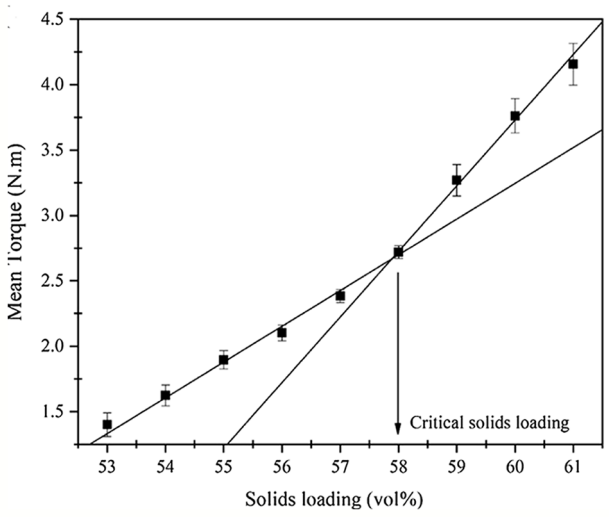

Figure 4. Mean torque values versus solids loading [21].

tion) parameter. This parameter is used for defining the packing density of a certain powder particle in a liquid or melted mixture [22-25]. Modified oil absorption test is used to determine CPVC according to ASTM D-28-31 [26]. The critical powder volume content (CPVC) and powder particle size are inversely related to each other, so that, by increasing the powder particle size the CPVC decreases. Also the particle size distribution affects the critical solids loading. By increasing the particle size distribution, the critical solids loading increases [27,28].

Simulation of filling stage

Mold filling simulations are performed using computational fluid dynamics principles based on the solution of motion, mass and energy stability equations (Navier-Stokes equations). These equations describe the flow motion under non-isothermal conditions. The following equations show the continuity and momentum balance equations [16]:

$$\nabla.u = 0 \quad and \quad -\nabla p + \nabla.\left(2\eta D\right) = 0 \qquad (1)$$

Where η, D, p, and u are the viscosity, rate of deformation tensor, pressure, and velocity, respectively. A function of the shear rate γ, temperature T, and pressure p is used to show the viscosity.

One of viscosity models used in PIM is the Cross-WLF (Williams–Ladel–Ferry) model, which is described as follows [16]:

$$\eta\left(\dot{\gamma}, T, p\right) = \frac{\eta_0}{1+\left(\frac{\eta_0 \gamma}{\tau^*}\right)^{1-n}} \qquad (2)$$

In this equation η0 represents the zero-shear-rate viscosity described by the WLF model, given by [16]:

$$\eta_0 = D_1 \exp\left[-\frac{A_1\left(T - T^*\right)}{A_2 + T - T^*}\right] \quad (3)$$

Where $A_2 = \tilde{A}_2 + D_3 p$ and T^* is the glass transition temperature of the polymer, and the materials parameters, A_1, $\tilde{A}_2$, D_1, D_2, and D_3, are determined by curve-fitting using the experimental viscosity data [16].

In the filling and packing simulation the pressure and energy equations must be solved during the cycle of filling and packing. This can be obtained by finite element method (FEM) for the Poisson equation and energy equation, however, in the thickness direction the finite difference method (FDM) is employed. Faced with complex geometries and irregular boundaries, the FEM shows excellent flexibility.

Drummer et al. [8] investigated the injection molding simulation of Alumina and zirconia feedstocks. They used Cross-WLF and Cross-WLF with Herschel Bulkley models to study the filling pattern in simulation. They mentioned that the coefficients that are used for Cross WLF with Herschel-Bulkley model cannot be read by Moldflow simulation Synergy 2013 from the Autodesk GmbH, and resulted that the effect of modeling and filling pattern cannot be analyzed. Figure 5 shows the viscosity curves of alumina and zirconia and the scales of shear rate where the model Cross-WLF with Herschel Bulkley can influence the flowing pattern. As it can be seen after 6% filling of alumina only the melt surface which does not touch the mold wall is affected by Herschel-Bulkley. When the melt reaches to the wall of the mold the shear rate will be too high to be affected by Herschel-Bulkley. Colors showed that Herschel-Bulkley had more influence on zirconia than alumina.

Inhomogeneity of the brown part and final part is resulted from separation of powder and binder which is a crucial matter in PIM process [29]. Mannschatz et al. mentioned that by increasing powder content the separation effects are reduced [30]. The phase separation phenomena could be detected by X-ray computed tomography CT, which includes 3D and the non-destructive characterization of the spatial structure [31-33]. The impact of filling patterns on the separation phenomenon is investigated by Wei et al. [29]. In order to simulate the mold filling, ANSYS-CFX 13 software was used. Based on the mold filling model, they stated that temperature of feedstock, shear rate, and drag coefficient are some of the factors which can affect the powder–binder separation. The separation phenomenon becomes more severe by increasing the temperature, which leads to the decrease of the feedstock viscosity. In fact, when the temperature increases, the amount of powder at the bottom reduces as shown in Figure 6. Increasing the injection rate leads to a more serious inhomogeneity. They stated that the impact of injection rate on filling patterns is smaller than the impact of temperature, because this parameter has smaller effect on viscosity.

Sudip et al. [34] investigated the simulation of separation phenomenon by developing a non-isothermal

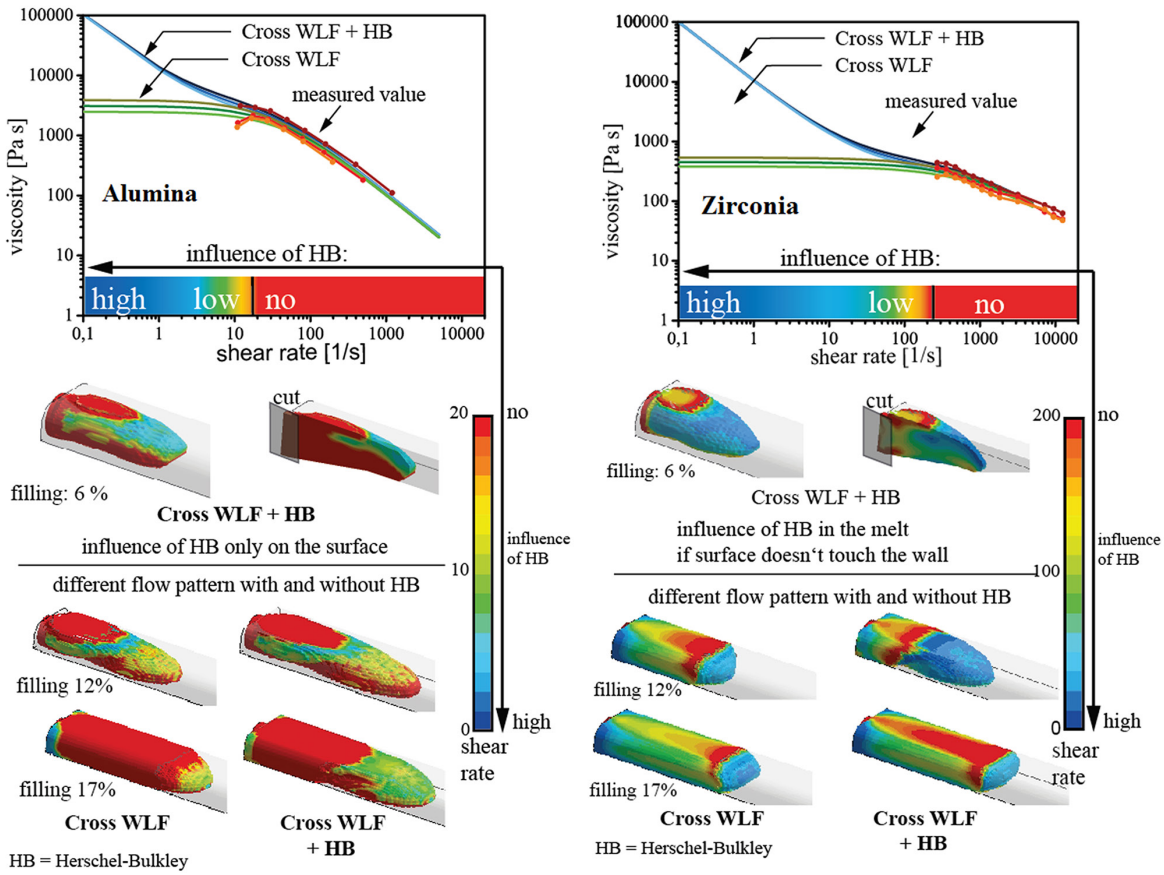

Figure 5. Filling pattern of the early stages of runner filling at the beginning of filling the runner - areas influenced by Cross WLF with Herschel-Bulkley [8].

multiphase flow numerical model. They reported that phase segregation is more sensitive to injection temperature in comparison to the injection speed, which is due to the greater effect of temperature on viscosity.

Tosello et al. [35] studied the simulation performance validations of ceramic injection molding process. In their study the required data for establishing a material model are introduced. They discussed the essential measurements and tools according to the powder content.

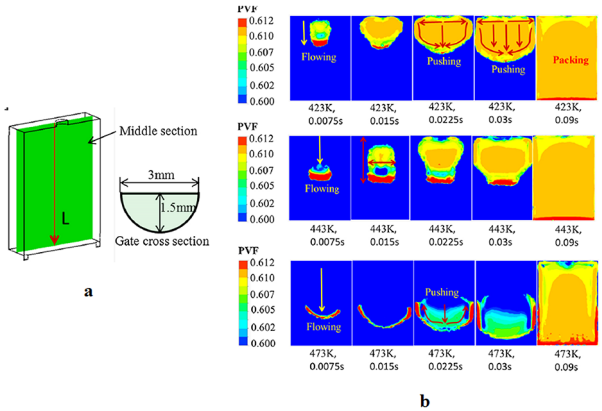

Figure 6. a) Gate cross-section size and middle section, b) progress of the powder value in the middle section at various temperatures and injection rate of 60 $cm^3.s-1$[29].

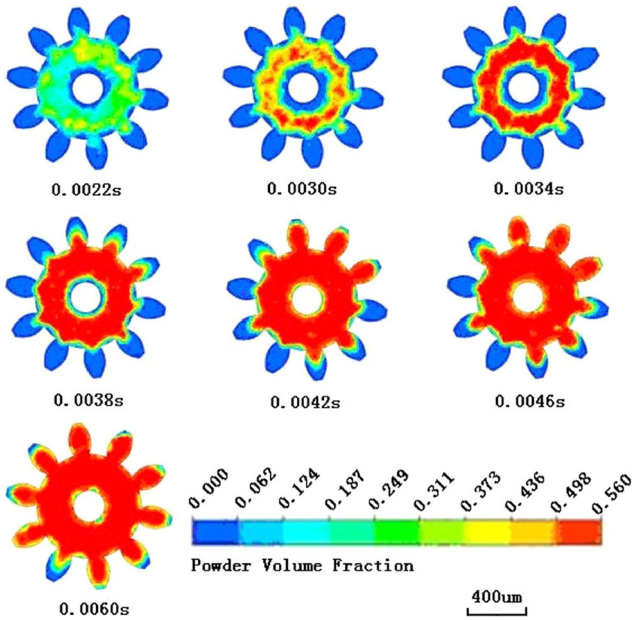

Figure 7. Filling of the upper surface of the gearwheel cavity with the addendum circle of 900 μm at various times [36].

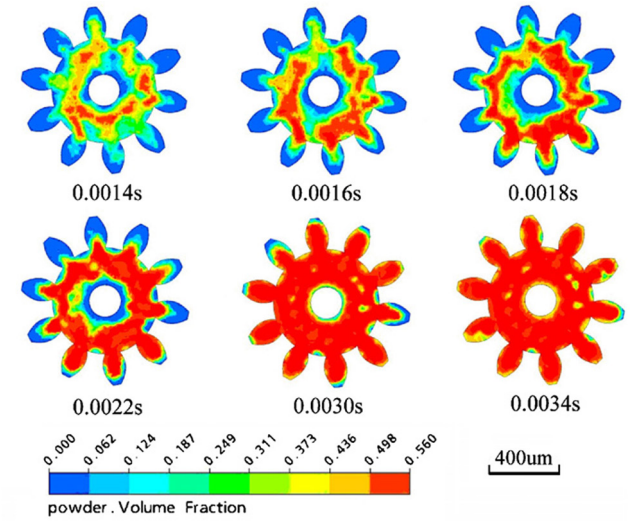

Figure 8. Filling simulation of a cavity far from the gate for a gearwheel [36].

Yin et al. [36] simulated the mold filling stage of carbonyl iron feedstock by ANSYS CFX software. They reported that inhomogeneity affects the shape precision of the micro-sized parts. According to Figurs 7 and 8, better moldability is seen for the cavity away from the gate compared to that one near the gate. They reported that changes in the mode of mold filling and heat exchange can result in some differences in shape quality of the molded compact [36].

Sardarian et al. [37] simulated the filling step of aluminum by Moldflow Synergy (Autodesk) software. The low pressure injection molding (LPIM) process was used instead of high pressure injection molding (HPIM), which needs much smaller pressure and temperature values. In their study the required pressure versus temperature for filling the molds is correctly simulated. They observed different flow patterns in top and side views, since the pattern in top view is like a bubble swollen with melt this pattern is called fountain flow or bubble flow (Figure 9). Actually, in practice, gravity pulled the melt front to the bottom of the cavity while simulation assumes a fountain flow pattern.

In another work, Sardarian et al. [38] measured the bulk density and four point flexural strength of the parts produced by LPIM and simulated the filling stage of alumina by finite element method (FEM). They reported that by increasing the injection velocity over a critical value, jetting phenomenon during the filling of cavity can be happened. They estimated that this phenomenon leads to lots of voids in the final part. Figures 10 and 11 show the mold cavity filling and simulation of mold cavity filling at temperature of 70°C and pressure of 0.1 MPa for the uniform filling and at temperature of 100°C and pressure of 0.6 MPa for the jetting fill, respectively.

The effect of inhomogeneity in nano zirconia powder is investigated by Jianqiao et al. [39]. Simulation results showed that the powder velocity in front of the gate and around the corner near the gate are, respectively, very high and slow as shown in Figure 12. Authors expressed that this is due to the drop of injection pressure during mold filling.

Hao et al. [40] simulated the filling process of stainless steel powder by the granular modeling. This model can predict the density distribution in all zones of a mold. They used two isosceles triangle molds, as can be seen from Figure 13 one of them has a barrier in its center and the other has a thin step in its front.

They investigated the impact of various injection factors and resulted that by increasing the injection pressure and velocity, the flow of powder particles increases. They stated that it is very hard to fill the tip of the triangle and this problem can be solved by increasing the injection pressures and velocities (Figure 14). This model provides solutions for understanding the filling

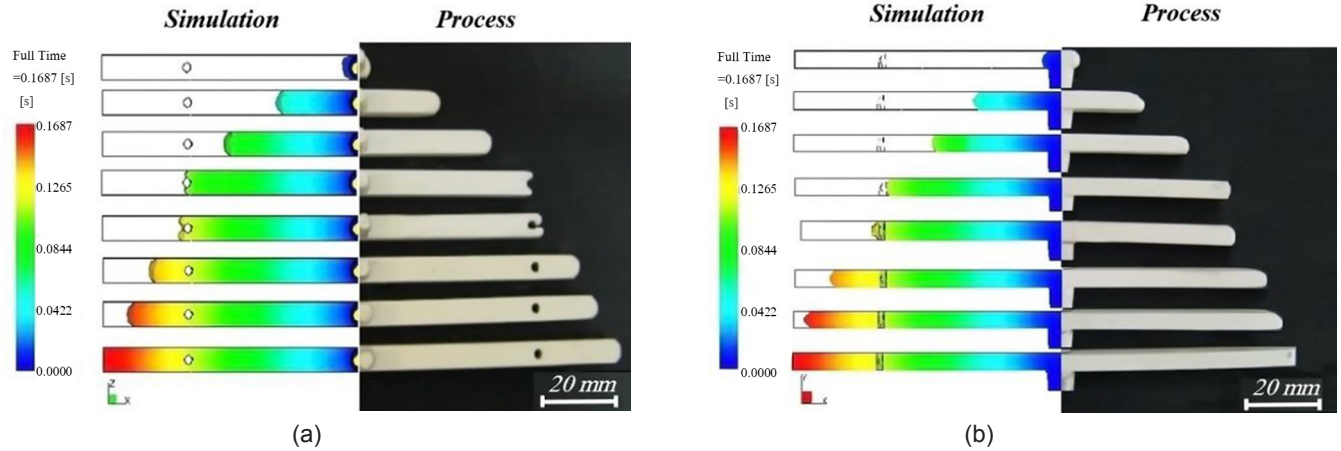

Figure 9. (a) Top and (b) side views of the simulation and injected part [37].

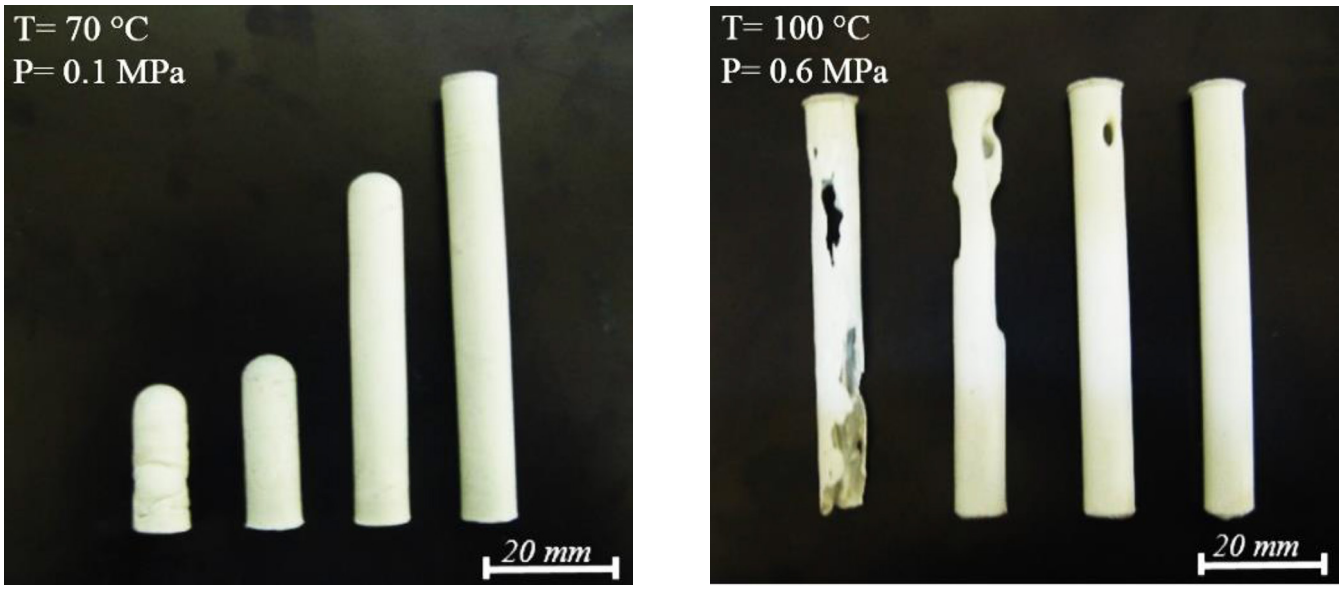

(a) (b)

Figure 10. Filling stage of alumina feedstock (a) uniform filling; (b) jetting phenomenon [38].

stage and mechanisms of powder transformation. Besides, it can determine an improved numerical tool for optimizing mold design and injection parameters.

Matula et al. simulated polymer-powder slurry injection by Cadmould 3D-F software tool [41]. This program is capable to analyze the injection point location, distribution of pressure, filling and packing, cooling system, and so on. Authors used the Carreau- WLF model for their simulation. Plots of viscosity versus shear rate are used to determine the required parameters. The model they used is presented in Figure 15. From Figurs 16 and 17, they deduced that the required pressure for filling the cavity and mold clamping force in the polymer-powder mixture are lower than molding other composites or pure high-density polyethylene alone.

Simulation and modeling of debinding stage

After the green body is made (the injected part), it should be debinded. Since the remaining binders act as pollutant elements in the sintered parts, the binders must be removed [42,43]. Incomplete removal of the binder may leads to distortions, non-uniform shrinkage, cracks, warping, and voids in the final part [44-46]. Besides, in order to maintain the shape of the product before the sintering stage, a small amount of backbone binder is needed [42,47]. Binder removal can be performed by several various methods, such as; catalytic

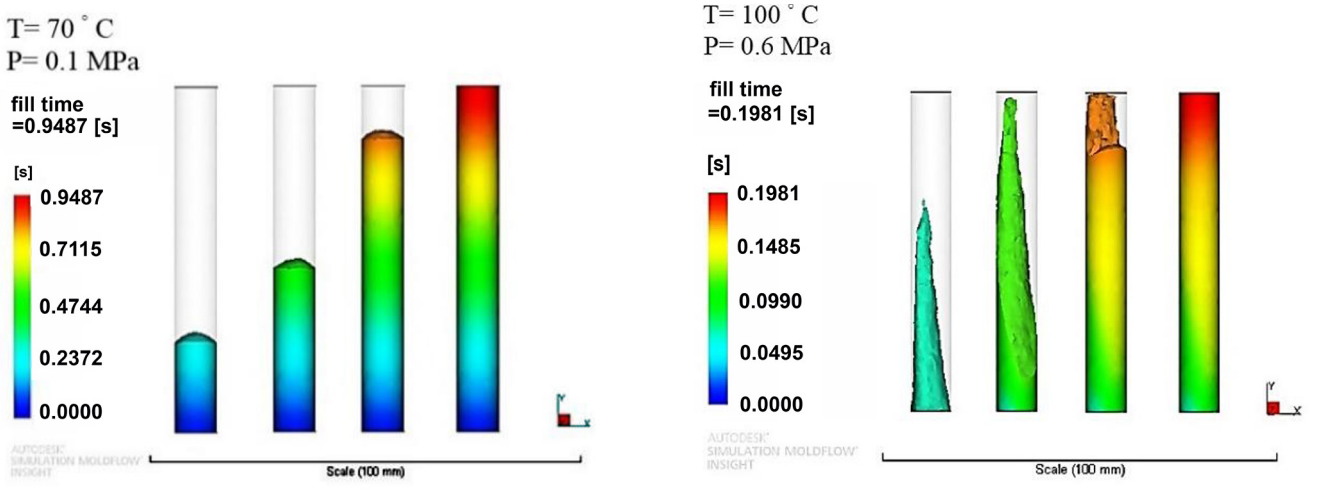

(a) (b)

Figure 11. Simulation filling stage of alumina feedstock (a) uniform filling; (b) jetting phenomenon [38].

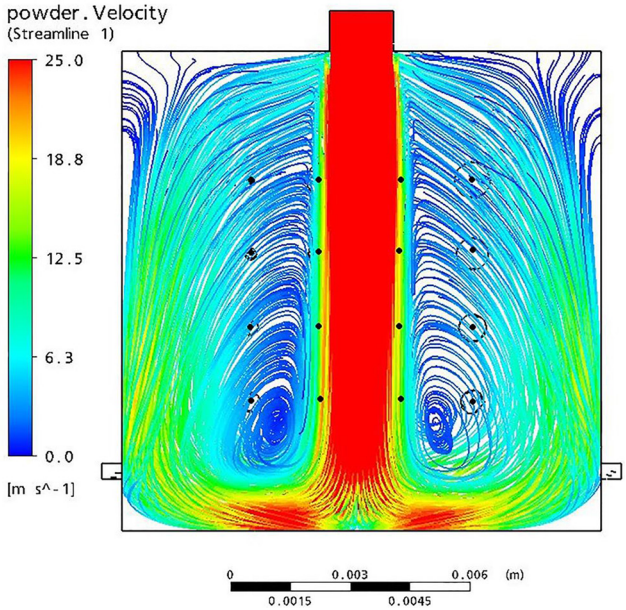

Figure 12. Powder velocity related to the filling path in the cavity [39].

debinding, thermal debinding, solvent debinding and wicking debinding [48-50]. Thermal debinding is the most time-consuming process. During binder removal, it is essential for the feedstock to have high yield stress and shows steady thermal degradation properties to maintain the shape of the part [51].

By computer simulations the time needed for debinding process can be decreased. Several researches have

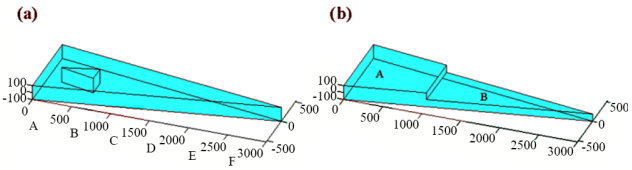

Figure 13. Schematics of molds for simulation and validation of experiments: (a) mold with barrier and (b) mold with thin step (unit: μm) [40].

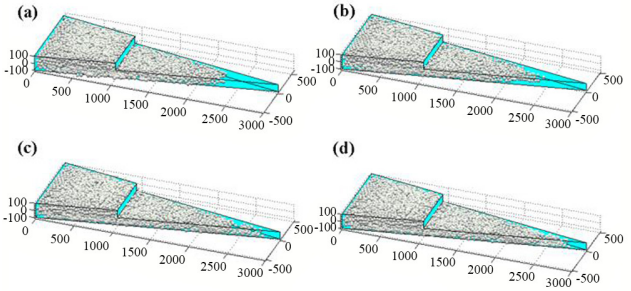

Figure 14. Filling simulation of the mold with a step in its tip at various injection pressures and velocities: (a) 90 MPa, 6 m/s; (b) 90 MPa, 12 m/s; (c) 180 MPa, 6 m/s, and (d) 180MPa, 12 m/s [40].

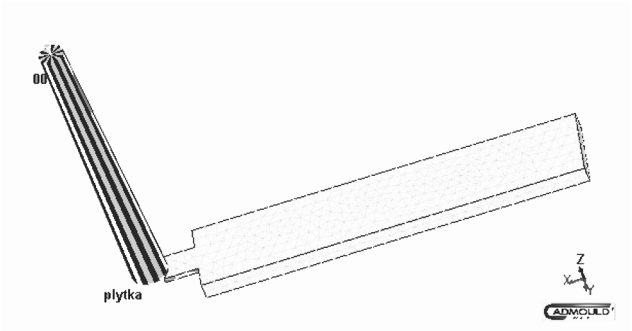

Figure 15. Model of the mold cavity and the channel which provides the material [41].

been investigated the simulation of debinding step [52-58]. Debinding process should be optimized carefully, because too slow or too fast debinding makes different problems. Master decomposition curve (MDC) model is one of the proposed models to describe the debinding process [29]. This model helps to predict the amount of the residual binder by the minimum set of tests. Won et al. used MDC model to study the binder removal in a bimodal feedstock [59].

Park et al. stated that the weight fraction of a binder can be written as follow [60]:

$$-d\alpha/dt = \alpha\, k_0 \exp(-Q/RT) \quad (4)$$

Where α is the weight fraction, k0 is the specific rate constant of thermal degradation. Q, R and T are the decomposition activation energy, gas constant, and absolute temperature, respectively. If the heating rate is constant, the equation can be written as [60]:

$$Q_r/RT_{max}^2 = K_0 \exp(-Q/RTmax) \quad (5)$$

Where r is the heating rate and T_{max} is the temperature where the maximum rate of weight loss happens. Slope of ln (r/T^2_{max}) vs. ln $(-1/RT_{max})$ graph shows decomposition activation energy.

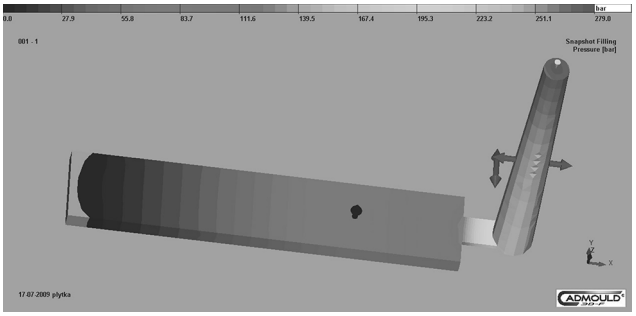

Figure 16. Distribution of pressure for T15/HD-PE/PW composite (after 98% filling) [41].

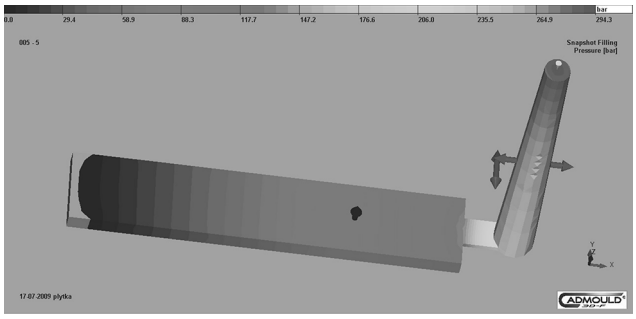

Figure 17. Distribution of pressure for difficult flowing HDPE (after 98% filling) [41].

Binder system consists filler, backbone polymer, and surfactant. Therefore, when MDC model is applied for binder system, it is necessary to consider the multi reaction steps.

Park et al. [60] resulted that the feedstock containing nano powder needs higher immersion time for solvent debinding. Nano powder also affected the thermal debinding behavior. They reported that the activation energy of PW and SA will be increased by increasing the ratio of nano powder, while, the energy of PP and PE will be decreased. The lowest necessary energy to initiate the pyrolysis of binder is decomposition activation energy, so the higher the activation energy of the binder, the higher the decomposition temperature. Therefore, by adding or increasing the amount of nano powder, the debinding process became more challenging.

Mamen et al. [61] investigated the thermal debinding process of fine powder 316L stainless steel and adopted the data from experimental tests and simulations to identify the kinetic parameters. In order to evaluate these parameters the Kissinger and Ozawa methods were used. For the simulation of thermal debinding stage, they developed a mathematical model. Comsol Multiphysics® software was employed to determine the distribution of remaining binder. Also by this software any physical process described with partial differential equations (PDE) can be simulated. In their study as shown in Figure 18 by increasing the debinding temperature, the rate of polymer elimination is increased rapidly and then slows down when the debinding temperature is around 410°C. They expressed that diffusion of the polymer is more effective in the limitation of debinding rate than degradation of the polymer. In the initial step since the distance of polymer diffusion is short the debinding is occurred rapidly. As the process progresses, the pore channels are extended to the internal areas of the compact and

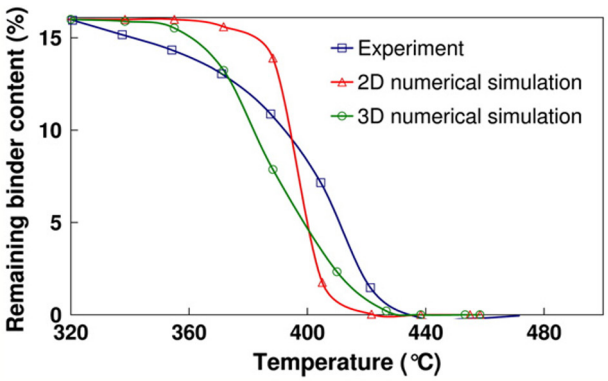

Figure 18. Rate of polymer elimination versus debinding temperature for fine 316L stainless steel feedstock [61].

long way of the diffusion leads to the reduction of the debinding rate.

In Mamen study, experimental results showed better adoption with 3D simulation than 2D simulation, because in reality there are some outer surfaces that polymer uses to exit the sample which in 2D simulation are ignored.

Figure 19 shows the 2D and 3D simulations of the distribution of residual polypropylene at 385°C; at this debinding temperature weight loss is happened quickly. Continuous changes of distribution from surface to the center of the compact are shown.

Somasundram et. al. [62] investigated the 2-D simulation of wick debinding for ceramic parts in close proximity. In wick debinding process the part is plunged in the powder with fine pores. When the temperature rises, the binder melts and removes from the part by capillary suction pressure, which is named wicking. Debinding in a wicking embedment helps avoiding the formation of defects [63]. After this process the part is partially debinded and contains developed open porosities. Binder removal will be completed during sintering, which the residual binder burns and evaporates [63].

Somasundram et.al. [62] used the model they have presented in 2008 [64] and simulated the isothermal

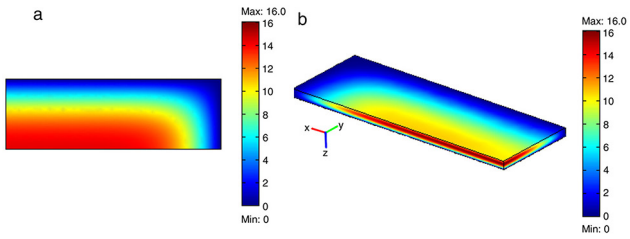

Figure 19. (a) 2D and (b) 3D simulations of the distribution of residual polypropylene at 385 °C [61].

debinding of cylindrical parts which were placed close to each other. They solved the PDE of equation (6) for one dimensional case by COMSOL Multiphysics (Version 3.3a, COMSOL, Inc.), which is a commercial finite element method software package, and simulated the motion of binder front in the wicking powder. They claimed that the simulation takes less than 10s on a standard 3 GB RAM PC and 2.41GHz processor. Equation (6) is [64]:

$$A\,\partial p/\partial t = \partial/\partial Z\,(B/\mu\,\partial p/\partial Z) \quad (6)$$

Where A and B are coefficients, z is the axial dimension (direction of debinding), μ is the binder viscosity and p is the capillary pressure.

They stated that when the parts are placed close together the wick debinding rate decreases. Narrow separation causes that the binder fronts collide early and results in the reduction of the suction of wicking powder on the binder. In Figure 20 the encounter of the two fronts after 2h is shown. After that the debinding is occurred in the upward direction.

Simulation of sintering step

Mechanical and physical properties of the components produced by powder injection molding are strongly dependent on the sintering step. In sintering step the essential mechanical properties of the final product is achieved through bonding the mechanical properties together. In this stage a large shrinkage of 10-20% will be occurred, so it is very important to control the dimensional changes and distortions [65]. Generally, in the sintered PIM components the relative density of produced part is greater than 95% [66]. Continuum models which are based on the theories of plastic and viscous flow are used to explain the densification of the part during sintering [67]. Significant attempts have been performed to develop simulations and modeling of sintering stage and grain growth powders [65, 67-73]. Mamen et al. investigated the sintering behavior of fine and coarse tungsten parts produced by injection molding process in a Setaram© analyzer under the stream of hydrogen with high purity and temperatures up to 1700°C [66]. Continuum sintering model was used to predict the final shrinkage and density distribution in the final product. This model has been performed in ABAQUS software via the user subroutine UMAT. They investigated the impact of powder particle size on the densification behavior, sintering activation energy, and sintering stress. Various macroscopic models are created to simulate the shrinkage and distortion in this stage. In sintering stage the total strain can be determined by the following equation [74]:

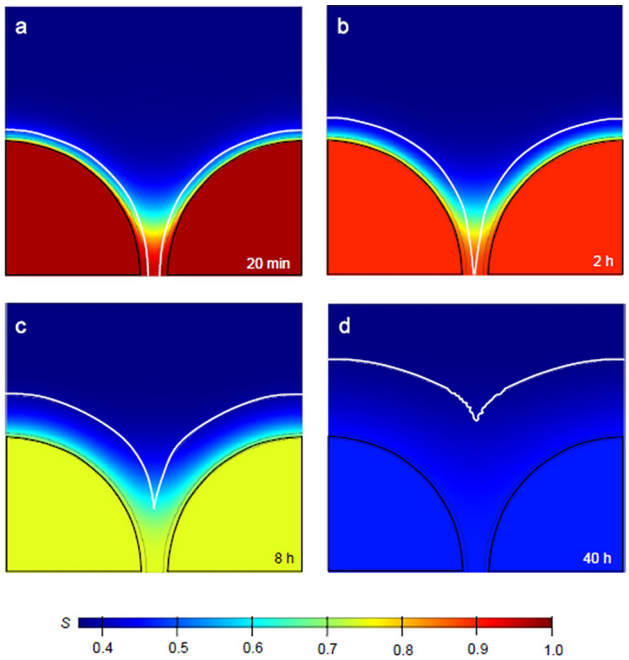

Figure 20. Saturation progress in the parts and the pressure in wicking powder for cylindrical rods with 2mm gap. White line indicates binder front in wicking powder. Simulated times are (a) 30 min, (b) 2 h; (c) 8 h; and (d) 40 h [64].

$$\dot{\varepsilon} = \dot{\varepsilon}_e + \dot{\varepsilon}_{th} + \dot{\varepsilon}_{vp} \quad (7)$$

Where, $\dot{\varepsilon}_e$, $\dot{\varepsilon}_{vp}$, $\dot{\varepsilon}$, and $\dot{\varepsilon}_{th}$, are the rate of elastic strain, viscoplastic strain, total strain, and thermal strain, respectively.

Viscosity of the components during isothermal sintering is as follow [75]:

$$\eta_P = \frac{KTG^3p^2}{47.5V_a\delta_b D_{b0}\exp\left(-Q_b/RT\right)} \quad (8)$$

In this equation T, G, R, and Qb are absolute temperature, grain size, gas constant, and the activation energy for grain boundary diffusion, respectively. V_a, D_{b0}, δ_b and k are material parameters which are assumed to be constant during process.

Following equation is used to determine the viscosity during non-isothermal sintering [76]:

$$\eta_P = \frac{1}{\dot{\delta}}\left(\frac{5p_0gL_s^4}{32h^2} + \frac{pL_s^3}{4bh^3}\right) \quad (9)$$

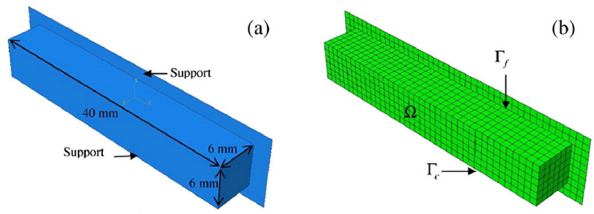

Figure 21. (a) Geometry of the support plate before sintering, (b) finite element model [66].

Where, g, b, h, δ, ρ, η_p, and P are gravity acceleration, width, thickness, deflection rate at the center of the specimen, initial relative density after the pre-sintering step, uniaxial viscosity, and external load, respectively.

Figure 21 shows the support and the component geometry which Mamen employed to create the model. The final relative densities of various sintered samples made from fine and coarse tungsten powders are shown in Figure 22a. They reported that both types of powders have homogeneous final relative densities. Figure 22b shows the ultimate shrinkages of the sintered components of the same powders. They resulted that the powder particle size affects the sintering behavior. Some parameters such as pores, friction between the support and component, and gravity have induced some errors in the coarse powders, which

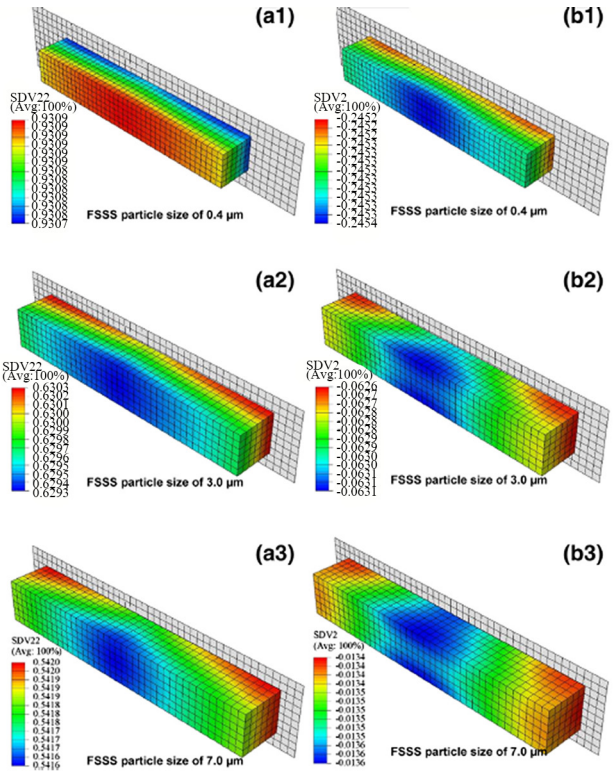

Figure 22. (a) Final relative density of sintered parts, (b) shrinkage of the sintered components [66].

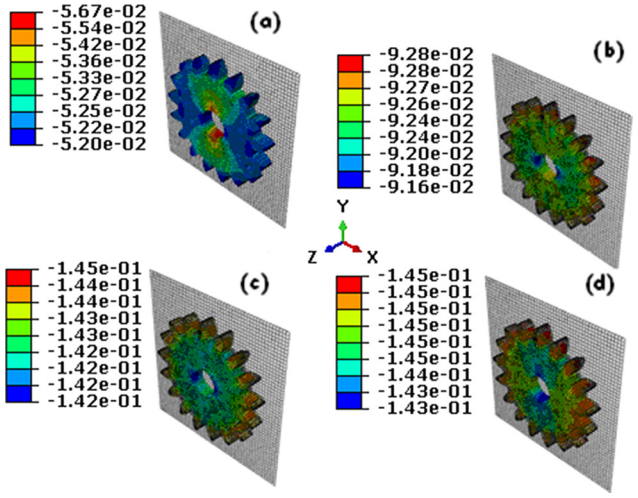

Figure 23. Numerical final shrinkage of the sintered micro-gears versus sintering temperature: a 1,050 °C, b 1,150 °C, c 1,250 °C and d 1,360 °C (heating rate, 10 °C/min, solid loading of 64 %, unit %) [77].

caused differences between numerical simulation and the experimental results.

Sahli et al. [77] investigated the numerical simulation of macroscopic deformation and structural evolution during sintering of 316 L stainless steel micro-parts manufactured by metal injection molding. They proposed a sintering model according to the elastic–viscoplastic equations and identified bulk viscosity, sintering stress and shearing viscosity by means of dilatometer experimental data. Then the model was performed into the finite element software to conduct the sintering simulation.

The numerical predictions of shrinkages and densities were compared with experimental measurements, and it is shown that the results numerically simulated by finite element agree well with those experimentally observed. The experimental data were obtained from sintering of stainless steel powders. They also predicted the mechanical properties of micro-gears before sintering by employing finite element (FE) methods. Distribution of the predicted numerical shrinkage of the parts after sintering at various temperatures is given in Figure 23. It can be seen that by increasing the sintering temperature the shrinkage of the samples increases and the maximum shrinkage is observed at the tooth surfaces.

CONCLUSION

Due to the growing trend of using the injection mold-

ing process in the production of metal and ceramic components, different simulation tools used to predict the feedstock behavior at different stages of the process are reviewed by various researchers. Simulations of each step of the process from mixing to sintering are discussed.

In the mixing stage the importance of the homogeneity and rheological properties of the feedstock are investigated and it is noted that in a homogenous feedstock the segregation of powder and binder has the least value. Studies showed that in order to determine the homogeneity of the feedstock a combination of methods of scanning electron microscopy of distribution of powder and binder, ratio of feedstock weight loss during debinding, and pycnometric density of feedstock should be considered. In this step, proper solids loading has an important effect on homogeneity of feedstock and segregation of powder and binder.

In the filing stage the Cross-WLF and Cross-WLF with Herschel Bulkley models are needed to study the filling pattern in simulation. In this step, the pressure and energy equations must be solved during the cycle of filling and packing. This can be obtained by finite element method (FEM) for the Poisson equation and energy equation.

In the debinding stage master decomposition curve (MDC) model can be used to describe the debinding process. This model helps to predict the amount of the residual binder by the minimum set of tests.

Finally, in the sintering step the numerical predictions of shrinkages and densities are discussed.

REFERENCES

1. German RM, Animesh Bose (1997) Injection molding of metals and ceramics. Metal powder industries federation, Princeton, NJ, USA
2. Merhar JR (1990) Overview of metal injection moulding. Metal Powder Rep 45: 339-342
3. Zhang T, EvansJRG (1989) Predicting the viscosity of ceramic injection moulding suspensions. J Eur Ceram Soc 5: 165-172
4. Lin SP, & German RM (1994) The influence of powder loading and binder additive on the properties of alumina injection-moulding blends. J Mater Sci 29: 5367-5373
5. German RM (1994) Homogeneity effects on feedstock viscosity in powder injection molding. J Am Ceram Soc 77: 283-285
6. Piotter V (2011) A review of the current status of Micro PIM. Powder Inject. Molding Int 5: 27–42
7. Attia UM, Alcock JR (2011) A review of micropowder injection moulding as a microfabrication technique. J Micromech Microeng 21: 043001
8. Drummer D, Messingschlager S (2014) Ceramic injection molding material analysis, modeling and injection molding simulation. Proceedings of the 29th International Conference of the Polymer Processing.
9. Yu, PC, Li QF, Fuh JYH, Li T, Ho PW (2009) Micro injection molding of micro gear using nano-sized zirconia powder. Microsyst Technol 15: 401-406
10. Martin R, Vick M, Enneti RK, Atre SV (2013) Powder injection molding of ceria-stabilized, zirconia-toughened mullite parts for UAV engine components. JOM 65: 1388-1394
11. Martin R, Vick M, Kelly M, De Souza JP, Enneti RK, Atre SV (2013) Powder injection molding of mullite-zirconia composite. J Mater Res Techn 2: 263-268
12. Onbattuvelli V, Atre S (2011) Review of net shape fabrication of thermally conducting ceramics. Mater Manuf Process 26: 832-845
13. Onbattuvelli VP, Laddha S, Park SJ, De Souza JP, Atre SV (2011) SiC for the powder injection molding of thermal management devices. 66th ABM International Congress: 319-329
14. Kate KH, Enneti RK, McCabe T, Atre SV (2016) Simulations and injection molding experiments for aluminum nitride feedstock. Ceram Int 42: 194-203
15. Kang TG, Ahn S, Park SJ, Atre SV, German RM (2009) Mixing Simulation for Powder Injection Moulding Feedstock: Quantification and Sensitivity Analysis. PIM Int 3: 59-62
16. Donald F (2012) Handbook of metal injection molding. Woodhead Publishing Limited, Oxford, pp. 197–233
17. Alberto Naranjo, Juan F Campuzano, Iván López, (2017), Analysis of heat transfer coefficients and no-flow temperature in simulation of injection molding. SPE ANTEC, Anaheim
18. Tosello, G, Marhöfer DM, Islam A, Müller T, Plewa K, Piotter V (2019) Comprehensive characterization and material modeling for ceramic injection molding simulation performance validations.

Int J Adv Manufact Techn 102: 225-240
19. Raymond V (2012) Metal injection molding development: Modeling and numerical simulation of injection with experimental validation. Doctoral dissertation, École Polytechnique de Montréal
20. Jang JM, Lee H, Lee W, Kim YI, Ko SH, Kim JH, Choi JP (2014) Evaluation of feedstock for powder injection molding. JPN J Appl Phys 53: 05HA03
21. Askari A, Alaei MH, Omrani AM, Nekouee K, Park SJ (2019). Rheological and thermal characterization of AISI 4605 low-alloy steel feedstock for metal injection molding process. Metals Mater Int : 10.1007/s12540-019-00442-9
22. Abdoos H, Khorsand H, Yousefi AA (2014) Torque rheometry and rheological analysis of powder–polymer mixture for aluminum powder injection molding. Iranian Polym J 23: 745-755
23. Reddy JJ, Vijayakumar M, Mohan TRR, Ramakrishnar P (1996) Loading of solids in a liquid medium: Determination of CBVC by torque RHEOMETRY. J Europ Ceramic Soc 16:567–574
24. Sotomayor ME, Varez A, Levenfeld B (2010) Influence of powder particle size distribution on rheological properties of 316L powder injection molding feedstocks. Powder Tech 200: 30–36
25. Reddy JJ, Ravi N, Vijayakumar M (2000) A simple model for viscosity of powder injection moulding mixes with binder content above powder critical binder volume concentration. J Eur Ceram Soc 20: 2183–2190
26. Mutsuddy BC, Ford RG (1995) Ceramic injection molding. Chapman & Hall, London
27. Honek T, Hausnerova B, Saha P (2005) Relative viscosity models and their application to capillary flow data of highly filled hardmetal carbide powder compounds. Polym Compos 26: 30–36
28. Contreras JM, Jimenez-Morales A, & Torralba JM (2010) Experimental and theoretical methods for optimal solids loading calculation in MIM feedstocks fabricated from powders with different particle characteristics. Powder metall 53: 34-40
29. Fang W, He X, Zhang R, Yang S, Qu X (2014) The effects of filling patterns on the powder–binder separation in powder injection molding. Powder Technol 256: 367-376
30. Mannschatz A, Höhn S, Moritz T (2010) Powder-binder separation in injection moulded green parts. J Eur Ceram Soc 30: 2827-2832
31. Yang S, Zhang R, Qu X (2013) X-ray tomographic analysis of powder-binder separation in SiC green body. J Eur Ceram Soc 33: 2935-2941
32. Weber O, Rack A, Redenbach C, Schulz M, Wirjadi O (2011) Micropowder injection molding: Investigation of powder-binder separation using synchrotron-based microtomography and 3D image analysis. J Mater Sci 46: 3568-3573
33. Yang S, Xu Q, Liu C, Lu X, Qu X, Xu Y(2019) Analysis of powder binder separation through multiscale computed tomography. Metals 9: 329
34. Samanta SK, Chattopadhyay H, Godkhindi MM (2011) Modelling the powder binder separation in injection stage of PIM. Prog Comput Fluid Dy 11: 292-304
35. Tosello G, Marhöfer DM, Islam A, Müller T, Plewa K, Piotter V (2019) Comprehensive characterization and material modeling for ceramic injection molding simulation performance validations. Int J Adv Manuf Tech 102: 225-240
36. Yin H, Wang Q, Qu X, Jia C, Johnson JL (2011) Computational simulation and experimental analysis of the mold-filling process in μPIM. J Micromech Microeng 21: 045023
37. Sardarian M, Mirzaee O, Habibolahzadeh A (2017) Mold filling simulation of low pressure injection molding (LPIM) of alumina: Effect of temperature and pressure. Ceram Int 43: 28-34
38. Sardarian M, Mirzaee O, Habibolahzadeh A (2017) Numerical simulation and experimental investigation on jetting phenomenon in low pressure injection molding (LPIM) of alumina. J Mater Process Tech 243: 374-380
39. He J, Shao Z, Yin H, Elder S, Zheng Q, Qu X (2018) Investigation of inhomogeneity in powder injection molding of nano zirconia. Powder Technol 328: 207-214
40. He H, Li Y, Lou J, Li D, Liu C (2016) Prediction of density variation in powder injection moulding-filling process by using granular modeling with interstitial power-law fluid. Powder Technol. 1; 291:52-9
41. Matula G, Dobrzański LA, Ambroziak M (2012) Simulation of powder injection moulding conditions using cadmould program. JAMMFE 55: 556-560
42. Ani SM, Muchtar A, Muhamad N, Ghani JA (2014) Binder removal via a two-stage debinding

process for ceramic injection molding parts. Ceram Int 40: 2819-2824
43. Páez-Pavón A, Jiménez-Morales A, Santos TG, Quintino L, Torralba JM (2016) Influence of thermal debinding on the final properties of Fe–Si soft magnetic alloys for metal injection molding (MIM). J Magn Magn Mater 416: 342-347
44. Hidalgo J, Jiménez-Morales A, & Torralba JM (2012) Torque rheology of zircon feedstocks for powder injection moulding. J Eur Ceram Soc 32: 4063-4072
45. Sommer F, Walcher H, Kern F, Maetzig M, Gadow R (2014) Influence of feedstock preparation on ceramic injection molding and microstructural features of zirconia toughened alumina. J Eur Ceram Soc 34: 745-751
46. Ahn S, Park SJ, Lee S, Atre SV, German RM (2009) Effect of powders and binders on material properties and molding parameters in iron and stainless steel powder injection molding process. Powder Technol 193: 162-169
47. Bleyan D (2015) Binder system for powder injection moulding. Doctoral thesis, Tomas Bata University, Zlín
48. Bloemacher M, Weinand D (1997) CatamoldTM-a new direction for powder injection molding. J Mater Process Tech 63: 918-922
49. Zu YS, Lin ST (1997) Optimizing the mechanical properties of injection molded W4.9% Ni 2.1% Fe in debinding. J Mater Process Tech 71: 337-342
50. Pinwill IE, Edirisinghe MJ, Bevis MJ (1992) Development of temperature-heating rate diagrams for the pyrolytic removal of binder used for powder injection moulding. J Mater Sci 27: 4381-4388
51. Hausnerova B, Kuritka I, Bleyan D (2014) Polyolefin backbone substitution in binders for low temperature powder injection moulding feedstocks. Molecules 19: 2748-2760
52. Lam YC, Yu SCM, Tam KC, Shengjie Y (2000) Simulation of polymer removal from a powder injection molding compact by thermal debinding. Metall Mater Trans A 31: 2597-2606
53. Shengjie Y, Lam YC, Yu SCM, Tam KC (2001) Two-dimensional simulation of mass transport in polymer removal from a powder injection molding compact by thermal debinding. J Mater Res 16: 2436-2451
54. Heaney DF, Spina R (2007) Numerical analysis of debinding and sintering of MIM parts. J Mater Process Tech 191: 385-389
55. Shengjie Y, Lam YC, Yu SCM, Tam KC (2002) Thermal debinding modeling of mass transport and deformation in powder-injection molding compact. Metall Mater Trans B 33: 477-488
56. Lin TL, Hourng LW (2005) Investigation of wick debinding in metal injection molding: Numerical simulations by the random walk approach and experiments. Adv Powder Technol 16: 495-515
57. Chang CY (2003) Numerical simulation of two-dimensional wick debinding in metal powder injection molding. Adv Powder Technol 14: 177-194
58. Khoong LE, Lam YC, Chai JC, Jiang L, Ma J (2007) Numerical and experimental investigations on thermal debinding of polymeric binder of powder injection molding compact. Chem Eng Sci 62: 6927-6938
59. Oh JW, Lee WS, Park SJ (2018) Investigation and modeling of binder removal process in nano/micro bimodal powder injection molding. Int J Adv Manuf Tech 97: 4115-4126
60. Park SJ, Wu Y, Heaney DF, Zou X, Gai G, German RM (2009) Rheological and thermal debinding behaviors in titanium powder injection molding. Metall Mater Trans A 40: 215-222
61. Mamen B, Thierry B, Jean-Claude G (2013) Investigations on thermal debinding process for fine 316L stainless steel feedstocks and identification of kinetic parameters from coupling experiments and finite element simulations. Powder Technol 235:192-202
62. Somasundram IM, Cendrowicz A, Johns ML, Prajapati B, Wilson DI (2010) 2-D simulation of wick debinding for ceramic parts in close proximity. Chem Eng Sci 65: 5990-6000
63. Gorjan L, Dakskobler A (2010) Partial wick-debinding of low-pressure powder injection-moulded ceramic parts. J Eur Ceram Soc 30: 3013-3021
64. Somasundram IM, Cendrowicz A, Wilson DI, Johns ML (2008) Phenomenological study and modelling of wick debinding. Chem Eng Sci 63: 3802-3809
65. Song J, Barriere T, Liu B, Gelin JC (2007) Numerical simulation of sintering process in ceramic powder injection moulded components. AIP Conf

Proc 908: 1111-1116
66. Mamen B, Song J, Barriere T, Gelin JC (2015) Experimental and numerical analysis of the particle size effect on the densification behaviour of metal injection moulded tungsten parts during sintering. Powder Technol 270: 230-243
67. Blaine DC, German RM (2002) Sintering simulation of PIM stainless steel. Adv PM Part 10: 10-255
68. Lam YC, Chen X, Tam KC, Yu SCM (2003) Simulation of particle migration of powder-resin system in injection molding. J Manuf Sci Eng 125: 538-547
69. Kwon YS, Wu Y, Suri P, German RM (2004) Simulation of the sintering densification and shrinkage behavior of powder-injection-molded 17-4 PH stainless steel. Metall Mater Trans A 35: 257-263
70. Kong X, Quinard C, Barriere T, Gelin JC, Michel G (2009) Miniaturization & Nanopowders: Micro Injection Molding of 316L Stainless Steel Feedstock and Numerical Simulations. In European Congress and Exhibition on Powder Metallurgy, European PM Conference Proceedings (p. 1)
71. Song J, Gelin JC, Barrière T, Liu B (2006) Experiments and numerical modelling of solid state sintering for 316L stainless steel components. J Mater Process Tech 177: 352-355
72. Wu Y, Blaine D, Schlaefer C, Marx B, German RM (2002) Sintering densification and microstructural evolution of injection molding grade 17-4 PH stainless steel powder. Metall Mater Trans A 33: 2185-2194
73. German RM (2002) Computer modeling of sintering processes. Int J Powder Metall 38:48–66
74. Gasik M, Zhang BA (2000) Constitutive model and FE simulation for the sintering process of powder compacts. Comput Mater Sci 18: 93-101
75. Bordia RK, Scherer GW (1988) On constrained sintering-II. Comparison of constitutive models. Acta Metall 36: 2399-2409
76. Song J, Barriere T, Liu B, Gelin JC, Michel G (2010) Experimental and numerical analysis on sintering behaviours of injection moulded components in 316L stainless steel powder. Powder Metall 53: 295-304
77. Sahli M, Lebied A, Gelin J-C, Barrière T, Necib B (2015) Numerical simulation and experimental analysis of solid-state sintering response of 316 L stainless steelmicro-parts manufactured by metal injection molding. Int J Adv Manuf Tech 79: 2079–2092